


Reflective Polarization Volume Lens with Small f -Number and Large Diffraction Angle

Kun Yin, Ziqian He, and Shin-Tson Wu*

Planar optics based on patterned cholesteric liquid crystals (CLCs) has attracted increasing attention owing to the self-organized helical structure and the ability to create arbitrary reflected wavefront through spatial orientation control. However, because of the subwavelength-orientation requirement, it is challenging for liquid crystal lens to achieve a low f -number ($f/\#$) and large deflection angle simultaneously. Furthermore, with the increasing demand for compact size in novel optical systems, reflective lens has advantage over the transmissive one because it can fold the optical path. Here, a new off-axis reflective polarization volume lens (PVL) with $f/\# = 0.825$, large aperture size, simple fabrication process, thin profile, circular polarization selectivity, and large diffraction angle is proposed. In contrast to traditional vertical spiral structure, PVL is based on patterned CLCs with a slanted helical axis. In this paper, the PVL is theoretically evaluated and then three reflective PVLs at red, green, and blue wavelengths ($R = 605$ nm, $G = 532$ nm, and $B = 450$ nm) are fabricated. Meanwhile, a simple approach is utilized to achieve 20 mm diameter and 16.5 mm focal length. The low scattering and good image quality of reflective PVL enrich these functional devices and provide promising applications to novel foldable optical systems and waveguide-based wearable near-eye displays.

Photonic devices based on patterned cholesteric liquid crystals (CLCs) have attracted increasing attention because they are enablers of novel optical systems. A typical CLC device can realize liquid crystalline phase by self-organized molecules to form helical structure. If the circularly polarized light has the same handedness as the helical twist, the light propagating along the helical axis (z -axis) will experience Bragg reflection at normal incidence over the spectral range $2n_o\Lambda_B < \lambda < 2n_e\Lambda_B$, where Λ_B is the chiral period, and n_o and n_e are the ordinary and extraordinary refractive indices.^[1–4] Component with the opposite circular polarization will pass through the liquid crystal layer. By combining CLCs with the specially designed patterns in the horizontal (xy) plane, different optical devices can be created. For examples, if the phase profile is linearly varying, then the device behaves as a grating, and if the phase profile is parabolic,

K. Yin, Z. He, Prof. S.-T. Wu
College of Optics and Photonics
University of Central Florida
Orlando, FL 32816, USA
E-mail: swu@creol.ucf.edu

 The ORCID identification number(s) for the author(s) of this article can be found under <https://doi.org/10.1002/adom.202000170>.

DOI: 10.1002/adom.202000170

then it could function as a converging or diverging lens, depending on the incident circular polarization.^[3] Based on these attractive optical properties, many novel CLC devices have been developed and widely utilized in band pass filter,^[4] laser beam steering,^[5] optical combiners for augmented reality displays,^[6] optical vortex generators,^[7] beam shaper,^[8] and many broadband devices.^[9–11]

Previously, transmissive planar lenses, such as LC lens and metalens, along the optical axis of a symmetric structure have been developed.^[12–19] However, these lenses either have a small $f/\#$ but small size, or have a large aperture but large $f/\#$. As the demand for compact device structure keeps increasing, such a transmissive planar lens becomes too bulky and the reflective planar lens is urgently needed to provide foldable optical structure.

In this paper, we demonstrate a reflective polarization volume lens (rPVL) based on patterning slanted CLCs, exhibiting a large aperture and a small $f/\#$ ($=0.825$).

In an rPVL, ideally the incident light is primarily reflected and focused onto a specific off-angle. To obtain these functions, such a device requires both asymmetric subwavelength alignment and lens phase for achieving reflective off-axis imaging and an ultralow $f/\#$. In comparison with conventional transmissive planar lenses, our new rPVL with an $f/\# < 1$ and 45° off-axis diffraction angle is a critical enabler for future compact optical systems.^[20,21]

PVL is a combination of a slanted polarization volume grating (PVG) and a lens. In the past studies, the LC director distribution in a CLC device was often assumed planar without slanted helical axis. Because the bottom photoalignment is planar, which produces cholesterics with nearly zero pretilt angle; this means that the helical axis is perpendicular to the substrate. Until recently, some experimental evidences and rigorous analyses prove that the actual LC director configuration in a PVG is not planar; instead, it possesses slanted structure.^[22,23] Due to the trend of the lowest volume free energy, the helical axis of CLC bulk analyzed by the optimized Frank–Oseen model exhibits slanted rather than perpendicular to the substrate.^[23] Therefore, the helical axis of rPVL is also slanted, which differs from conventional CLC devices.

Figure 1a illustrates the schematic of the proposed rPVL. The substrate is treated to provide a rotation of LC optical axis in xy -plane, and the rotating angle changes continuously and

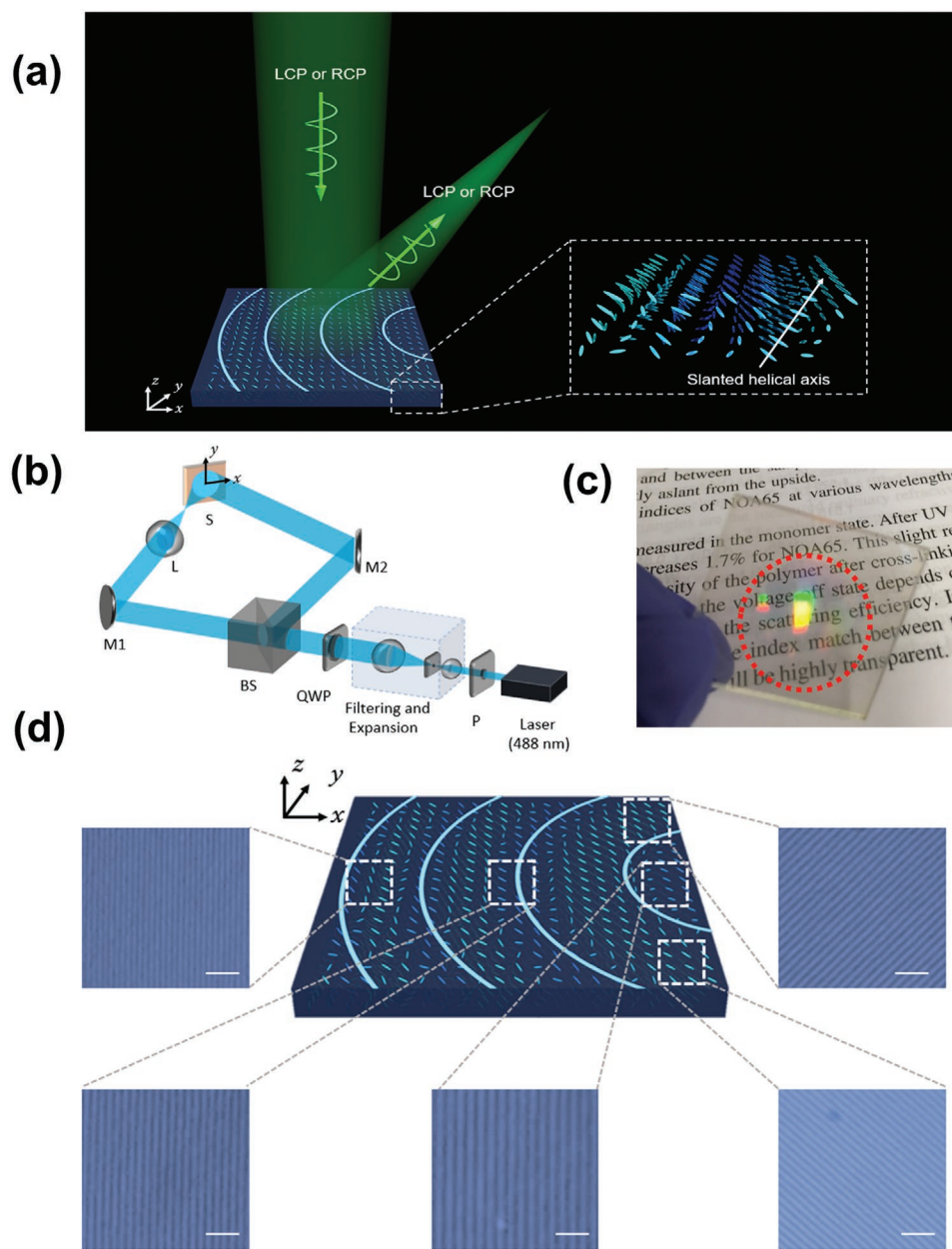


Figure 1. a) Schematic of the beam focus formed by an rPVL and the detailed LC director orientation inside the rPVL. b) Schematic of the optical exposure setup for fabricating rPVL. P: polarizer; QWP: quarter-wave plate; BS: beam splitter; M1 and M2: dielectric mirror; L: template lens; S: sample substrate. c) A photo taken through the sample. The rPVL region is circled by red dashed lines. The distance between PVL to camera is 15 cm, and the background is 5 cm away. The colorful image in the center of the rPVL is the image of the ceiling light. d) POM images of rPVL at three different locations. The size of each picture is $10 \mu\text{m} \times 10 \mu\text{m}$, and the scale bar is $2 \mu\text{m}$.

periodically to generate a lens-phase profile. When examining the detailed structure inside this device, the CLCs are precisely aligned in the horizontal plane and twisted in vertical direction along a slanted helical axis. At a macroscopic level, the rPVL has a parabolic phase profile, but when we zoom into a small area, the LC structure looks like a PVG with a linear phase profile. For a circularly polarized incident light (LCP or RCP) with the same handedness as the helical twist, the reflected beam from the rPVL is converged at an off-axis angle without changing its polarization state. The operation principle is equivalent to combining a reflective PVG with a convex lens for use as an off-axis

concave mirror: the incident light is converged by the lens profile and diffracted by the grating, thereby forming such a reflective off-axis focus.

To produce the desired continuously varying LC orientations of rPVL, we employed a modified Mach–Zehnder interferometer by photoinduced patterning. In general interference, when the two waves are orthogonally circularly polarized, the interfered standing wave is approximately linearly polarized everywhere with in-plane orientation $\Phi(x, y) = \Delta k \cdot r/2$, where Δk is the wavevector difference. This alignment technique has long been used for polarization grating fabrication, such

as PVG.^[24–28] Here, we insert an object (template lens) with phase $\varphi(x, y)$ in one beam to achieve the recording principle $\varphi(x, y) \rightarrow \Phi(x, y)$.^[15] Figure 1b shows the optical setup consisting of a laser, template lens, polarizer, beam splitter (BS), and rotatable wave plate. The incident laser beam ($\lambda = 488$ nm) is filtered and then expanded after passing through a linear polarizer. Then, the collimated linearly polarized beam is converted to circular polarization through a quarter-wave plate. After splitting into two arms by a nonpolarizing BS and being reflected by two dielectric mirrors, one beam is converted to LCP while the other is converted to RCP. Then, one beam is entering the template lens (L), the other is working as reference light. Therefore, the lens phase profile is generated at the substrate position. Then, the pattern is recorded on the prepared substrate (S), which is coated with a thin photoalignment film (Brilliant yellow). Because of the dichroic absorption, the molecules of photoalignment material tend to reorient their absorption oscillators perpendicular to the polarization direction of the illuminated light, and further orient LC molecules with an anchoring energy.^[17,29,30] To obtain the desired 45° diffraction angle for green light ($\lambda = 532$ nm), the interference angle between the two beams was $\alpha = 60^\circ$ to generate periodicity $\Lambda_x \approx 479$ nm at the center area.

Figure 1c shows the photos of the fabricated sample. We use an aspheric condenser lens with $f/\# = 0.7$ as the template to record the lens phase profile for rPVL. The thickness of the 25.4 mm aperture template lens is 14 mm and the focal length is 16 mm. As shown in Figure 1c, the rPVL region is circled by the red dashed lines and the size of the rPVL is 20 mm. It is worth mentioning that the diameter of the rPVL is limited by the size of the iris employed in the exposure setup, which can be significantly expanded by enlarging the iris and using a higher power laser. The photo taken under room light (at roughly 15° incident angle) shows the image of the ceiling light reflected by the sample. Due to the handedness selectivity, at the reflection band such an rPVL allows more than 50% transmission of the ambient light, and therefore the background can still be seen clearly.

To study the optical properties of the sample, we first inspect the surface pattern under a polarizing optical microscope (POM). As explained above, the rPVL shows the lens phase profile macroscopically and grating phase profile microscopically. For a small area, the radius of the curvature (around 1 cm) is too large to be observed compared to the scale of the period (several hundred nanometers), and the pattern is supposed to be line-shape rather than lens-shape. Figure 1d depicts the POM results of the fabricated rPVL. The scale bar is $2 \mu\text{m}$. As expected, the micropattern shows a line shape. The smallest period supporting the largest diffraction angle is 346 nm, the period of the middle area is 479 nm, and the largest period is 677 nm. When moving the sample along x -axis under POM, the periodicity gradually changes from 346 to 677 nm. To figure out the curvature, the sample was then translated along y -axis. The direction of the line-shape pattern ought to be changed gradually to generate the lens behavior and reach the maximum tilt angle at the edges. As shown in the right two pictures in Figure 1d, the direction of the lines is tilted almost 45° and the pattern is symmetric to the x -axis. This POM results confirm that each small area can be treated as a grating corresponding

to a particular diffraction angle and they work together to produce the off-axis focus.

Based on the observed real structure, we carry out a more in-depth theoretical analysis to reveal the physical principles of rPVL. As described, the PVL is a combination of diffractive grating and planar lens, both of which are inherently dispersive. Therefore, the chromatic aberrations in our rPVL are more pronounced than the lenses based on refractive optics, resulting in both wavelength-dependent focal length and diffraction angle. Figure 2a shows the schematic diagram of PVL and the position of the focal point is defined by the diffraction angle (β) and the focal length (f). For different positions on the PVL, the location-dependent diffraction angle can be expressed as $\beta(x, y)$. To simplify the calculation, we split the interference angle (α) into β_1 and β_0 , as illustrated in Figure 2b. The distance between the template lens and the sample is $2f_0$, and the exposed pattern phase can be expressed as

$$\Phi_0(x, y) = -k_r \sqrt{f_0^2 - 2xf_0 \sin \beta_0 + x^2 + y^2} + k_r x \sin \beta_1 \quad (1)$$

where k_r is the wavevector of the recording light ($\lambda_r = 488$ nm), and x and y are the coordinates. The parallel components of the grating K -vector can be further derived with

$$\begin{cases} K_x(x, y) = \frac{\partial \Phi_0}{\partial x} \\ K_y(x, y) = \frac{\partial \Phi_0}{\partial y} \end{cases} \quad (2)$$

To make sure the chief ray diffracts to the designed angle $\beta_d = \beta(0, 0)$, the norm of the grating K -vector is chosen to be $|K| = \sqrt{2}k_d n_a \sqrt{1 + \cos \beta_d}$, where k_d is the designed central wavevector ($\lambda_d = 532$ nm) and n_a is the average index of the PVL. Then the location-dependent diffraction angle between the grating K -vector and the z -axis can be expressed as $\gamma(x, y)$

$$\gamma(x, y) = \arcsin \frac{\sqrt{K_x^2 + K_y^2}}{|K|} \quad (3)$$

As shown in Figure 2a, for an incident light with wavevector k_i located in the bandgap of the PVG, its propagation satisfies the Bragg condition with diffraction angle $\beta(x, y) = 2\gamma(x, y)$ in the normal incidence and effective index $n_k(x, y) = k_d n_a \sqrt{1 + \cos \beta_d} / (\sqrt{2}k_i \cos \gamma(x, y))$. When the rPVL is placed in an environment with background index n_a , the diffracted beam follows the Snell's law and is refracted to a new diffraction angle $\beta'(x, y)$. In order to theoretically obtain the relationship between the diffraction angle $\beta(k_i)$, focus length $f(k_i)$, and the incident wavevector k_i , we compare the $\beta'(x, y)$ calculated from real structure with the diffraction angle $\bar{\beta}(x, y)$ of an ideal rPVL. Since the focal point is locating in xz -plane, $y = 0$

$$\begin{cases} \beta'(x, 0) = \arcsin \frac{n_k(x, 0)}{n_a} \sin \beta(x, 0) \\ \bar{\beta}(x, 0) = \arctan \frac{\bar{f} \sin \bar{\beta} - x}{\bar{f} \cos \bar{\beta}} \xrightarrow{\text{Taylor}} \bar{\beta}(x, 0) \approx \bar{\beta} - \frac{x \cos \bar{\beta}}{\bar{f}} \end{cases} \quad (4)$$

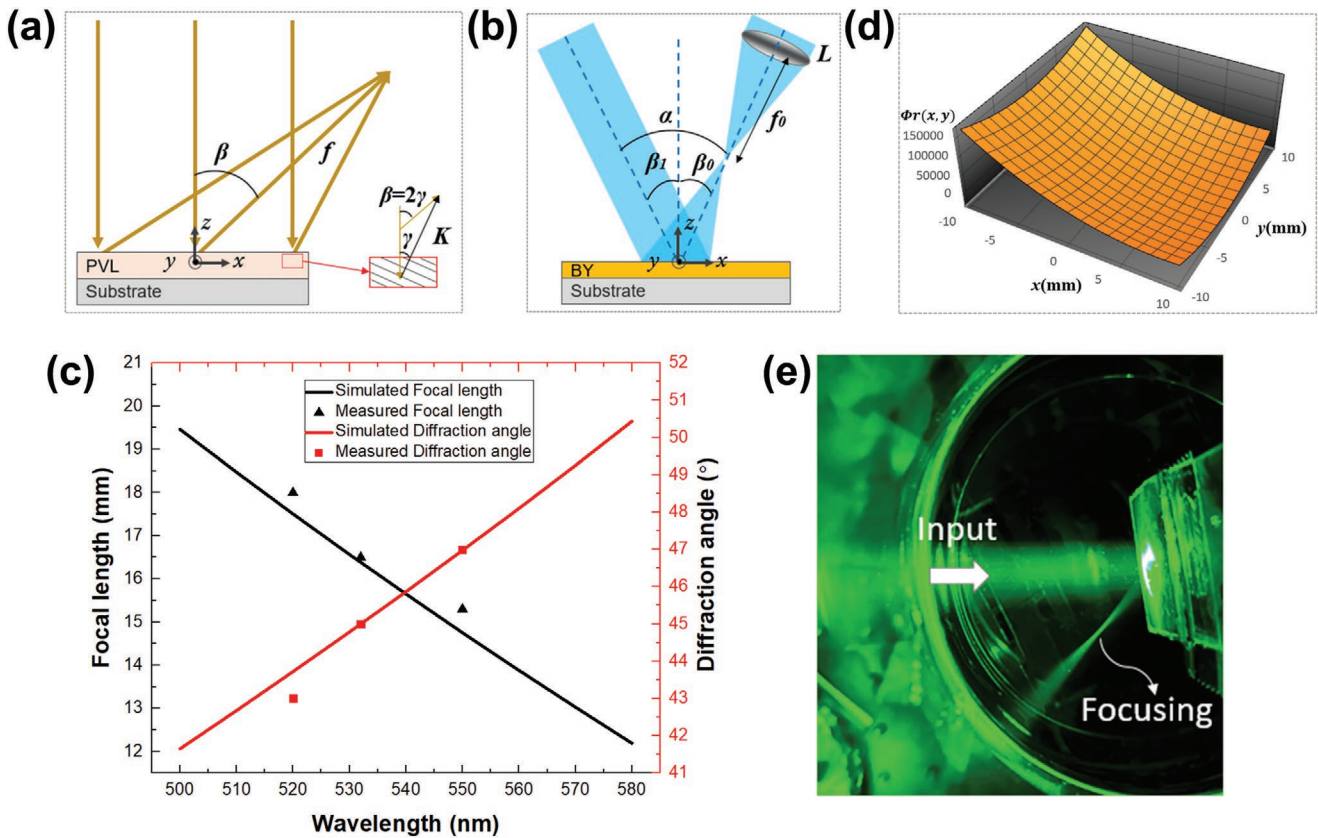


Figure 2. a) Schematic diagram showing the coordinates of the PVL. b) Schematic diagram showing the exposure parameters of the PVL. c) Simulated and measured results of the relationship between the focal point position and the incidence wavelength. d) The simulated diffractive phase of a 20 mm × 20 mm PVL. e) Sample immersed in a cylindrical container to observe the off-axis focusing behavior and diffraction angle.

Comparing each item in Equation (4), we derive the relationship of $\beta(k_i)$ and $f(k_i)$

$$\begin{cases} \bar{\beta}(k_i) = \arcsin \frac{k_d}{k_i} \sin \beta_d \\ \bar{f}(k_i) = f_0 \frac{n_a \sqrt{k_i^2 - \frac{k_d^2}{2} + \frac{k_d^2}{2} \cos 2\beta_d} \sqrt{1 - \frac{k_d^2}{k_i^2} \sin^2 \beta_d}}{k_r \cos^2 \beta_0} \end{cases} \quad (5)$$

As the incident wavelength shifts, both diffraction angle and focal length change caused by dispersion. To validate the simulation results, we use three different wavelengths ($\lambda_i = 520, 532,$ and 550 nm) to measure the focal lengths and the diffraction angles. As Figure 2c depicts, the solid lines represent the simulation results and dots are the measured data. The experimental results are in good agreement with the simulation. Then, we derive the phase of the diffractive light as following

$$\begin{cases} \Phi_r(x, y) = \int_{(0,0)}^{(x,y)} \vec{k}_r \cdot \vec{d}_r = \int_{(0,0)}^{(x,y)} (k_{r,x}, k_{r,y}) \cdot (d_x, d_y) \\ k_{r,x} = k_i n_k \sin \beta(x, y) \frac{K_x}{K_{||}} = \frac{k_i n_k K_x K_z}{|K|^2} \\ k_{r,y} = k_i n_k \sin \beta(x, y) \frac{K_y}{K_{||}} = \frac{k_i n_k K_y K_z}{|K|^2} \end{cases} \quad (6)$$

To intuitively understand the phase profile in Equation (6), we plot Φ_r in Figure 2d. The size is set to be 20 mm × 20 mm. The diffracted phase is supposed to change from 0 to 2π , however, the period is only several nanometers, which is too small to be observed in the range of 20 mm. Therefore, the phase is the accumulated phase, from 0 to 2π , and then from 2π to 4π , and so on. As Figure 2e depicts, we used an expanded and collimated green laser beam to observe the off-axis focusing behavior and the diffraction angle. The rPVL was fixed on a rotation stage and immersed to a glass cylindrical container filled with an index matching oil ($n = 1.58$). The incident light was perpendicular to the rPVL at the initial state. To change the diffraction angle, we can simply adjust the interference angle (α) in the exposure system. The smaller the angle (α), the smaller $f/\#$ can be obtained. Since the largest spatial frequency at the edge of the lens is smaller, in principle the on-axis lens can reach the smallest $f/\#$. In comparison with previous on-axis symmetric planar lens, our rPVL exhibits an asymmetric structure to generate both reflective and large off-angle images, which would definitely benefit the development of compact optical systems.

To further verify the practical use and optical performance of rPVL, three lenses designed for $R = 605$ nm, $G = 532$ nm, and $B = 450$ nm were fabricated and experimentally evaluated. To achieve same diffraction angle (45°), both the interference angle (α) and the concentration of chiral are redesigned. The detailed fabrication process is described in experiment part.

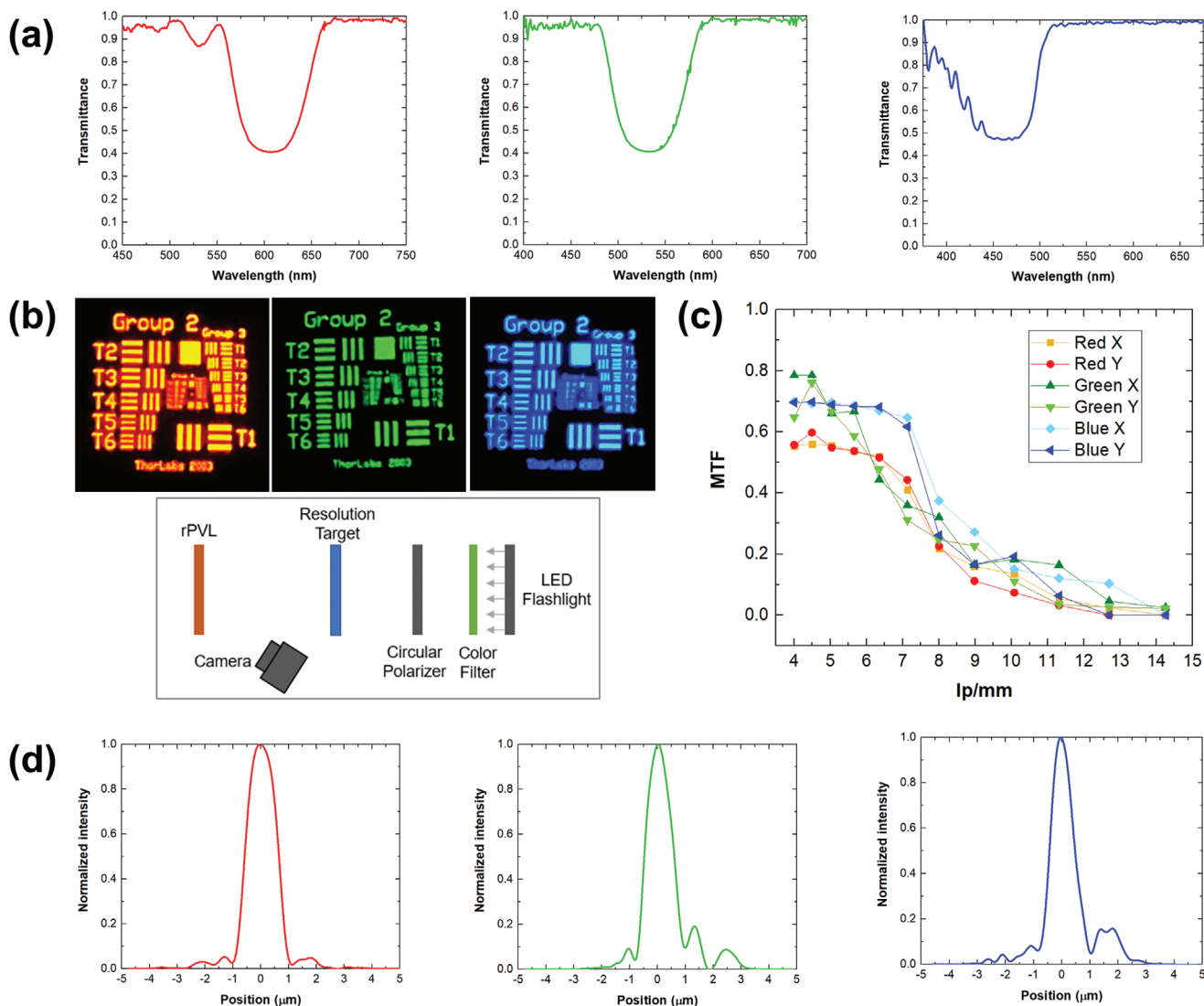


Figure 3. a) Measured transmission spectra with a circularly polarized light. The diffraction efficiency is plotted as a function of incident wavelength obtained from three rPVLs with the same $f/\#$ and different central wavelengths. b) The images of resolution test target with three rPVLs designed at $\lambda = 605, 532,$ and 450 nm and $f/\# = 0.825$, and the imaging experiment setup. c) The MTF drawn from the resolution target images. d) Measured focal spot intensity profiles.

Figure 3a depicts the measured transmission spectra of rPVLs with a circularly polarized light. The major contribution in transmission drop originates from beam diffracted of PVL, surface reflection, scattering, and absorption. While the former is centered at Bragg wavelength (here at 605, 532, and 450, respectively), the latter three usually have broader bandwidth and are very minimal. For the RGB rPVL, the measured efficiency is 60%, 60%, and 55%, respectively. Then, we measured the lens thickness by the surface profilometer and the result is 0.987, 0.991, and 0.827 μm for the RGB rPVL, respectively. The pitch length of our rPVL is about 300–400 nm. Normally, it would require about 10 pitches (i.e., 3–4 μm) to establish Bragg reflection and obtain 100% diffraction efficiency.^[31] However, our film is only about 1 μm thick, which corresponds to 2–3 pitches. Under such condition, the diffraction efficiency is $\approx 60\%$, which is in good agreement with our measured values.

Due to the limited uniformity and imprecise thickness control of our spin-coater, we can only prove the concept with 1 μm samples. By increasing the sample thickness, the efficiency will increase rapidly and then gradually saturates. To make a thicker rPVL, we could use a better thin-film machine to maintain the precise thickness control and minimize the surface roughness.

Then, the R1DS1N-Negative 1951 United State Air Force (USAF) resolution test target (Thorlabs Inc.) was used as the object to evaluate the imaging performance. We combined an LED flashlight with different color filters as RGB light sources. Because the rPVL operates based on a circularly polarized light, therefore, we added a circular polarizer after the color filter to improve the image quality. Images of the measured results and the experiment setup are shown in Figure 3b. For these three lenses, the smallest resolvable target is Group3 T6, which corresponds to 14.3 line pairs mm^{-1} , or linewidth $\approx 35 \mu\text{m}$. Based

on the images of the resolution test target, we process the data to obtain the modulation transfer function (MTF) information. Its values indicate the amount of detail in an image, given by the resolution of the optical system, and is customarily specified in line pairs per millimeter (lp mm^{-1}). A line pair is one cycle of a light bar and an adjacent dark bar of equal width. Figure 3c illustrates the MTF of RGB PVL in x and y directions. Figure 3d depicts the normalized intensity profile of the focal spots from the RGB rPVLs. The measured full-width half-maximum (FWHM) of the focal spot is 1.23, 1.10, and 0.91 μm , respectively. Comparing the FWHMs with the diffraction-limit ($\frac{\lambda}{2\text{NA}}$), the actual spot size is 2.5 \times larger than the theoretical values. The broadening of the focal spots should come from chromatic and monochromatic aberrations. As mentioned above, the PVL is inherently dispersive. Chromatic aberrations are more noticeable than the refractive optics, resulting in a wavelength-dependent focal length. The monochromatic aberrations result from the difference in the optical path length of the real ray between the real wavefront and the ideal wavefront. For a reflective PVL with small $f\#$ and large off-axis angle, the spherical aberration could be the most important factor that causes the broadening of focal spot. These two factors can be mitigated when PVL is used in a laser-based imaging system with wavefront corrections. In this condition, the linewidth and monochromatic aberrations induced broadening of the focal spot size would be suppressed.

In summary, various planar lenses are demonstrated following the diffractive optics concept of phase control based on a 2D plane. However, all of these are working on the on-axis transmissive type with either limited $f\#$ or small aperture size. In order to meet the needs of compact optical systems, we demonstrate a reflective planar lens with a low $f\#$, 20 mm diameter, and 45° diffraction angle in the visible region by using the patterning CLC method. The required subwavelength orientations for realizing an rPVL are achieved by incorporating interference exposure photoalignment and spin-coating method. The details of the surface including patterns and defects are observed by POM. Using the 1951 USAF resolution test chart, we have demonstrated red, green, and blue imaging in reflective and off-axis mode. Although our rPVL is subject to limited efficiency and resolution, the latter can be corrected with appropriate optical systems. Finally, the low-cost CLC device manufacturing capability makes our rPVLs suitable for widespread applications in novel foldable optical systems and integrated optics in the visible spectral region.

Experimental Section

Precursor Preparation: The rPVL precursor consisting of 2 wt% (working wavelength $\lambda = 532$ nm) chiral agent R5011 (HCCH, helical twisting power HTP $\approx 108 \mu\text{m}^{-1}$), 3 wt% initiator Irgacure 651, and 95 wt% photocurable monomer RM257 (HCCH) was diluted in toluene. The concentration of chiral dopant was 1.8, 2, and 2.4 wt% for red ($\lambda = 605$ nm), green ($\lambda = 532$ nm), and blue ($\lambda = 450$ nm), respectively.

Fabrication Process: To create subwavelength pattern on substrates, brilliant yellow (0.4 wt%) dissolved in dimethylformamide (DMF) was spin-coated onto a clean glass substrate at 800 rpm for 5 s and then 3000 rpm for 30 s as photoalignment layer. The substrate was then

subjected to the 488 nm interference exposure. The optical setup is shown in Figure 1b. The interference angle α was 53°, 60°, and 74° for red ($\lambda = 605$ nm), green ($\lambda = 532$ nm), and blue ($\lambda = 450$ nm), respectively. Then, the precursor was spin-coated onto the exposed substrates and cured with a UV lamp in nitrogen environment.

Optical Measurements: To characterize the transmission spectrum of rPVL, a white light source (Mikropack DH-2000) and an optical fiber spectrometer (Ocean Optics HR2000CG-UV-NIR) were used to achieve this measurement. The thickness of each sample was measured by a surface profilometer (Bruker DektakXT_2).

Acknowledgements

The authors would like to thank the Air Force Office of Scientific Research for the funding support (FA9550-14-1-0279), and Jianghao Xiong for helpful discussions.

Conflict of Interest

The authors declare no conflict of interest.

Keywords

Bragg gratings, cholesteric liquid crystals, metasurfaces, off-axis imaging, planar lens

Received: January 29, 2020

Revised: March 2, 2020

Published online:

- [1] M. Rafayelyan, G. Tkachenko, E. Brasselet, *Phys. Rev. Lett.* **2016**, *116*, 253902.
- [2] R. Barboza, U. Bortolozzo, M. G. Clerc, S. Residori, *Phys. Rev. Lett.* **2016**, *117*, 053903.
- [3] J. Kobashi, H. Yoshida, M. Ozaki, *Nat. Photonics* **2016**, *10*, 389.
- [4] Y. Huang, Y. Zhou, C. Doyle, S. T. Wu, *Opt. Express* **2006**, *14*, 1236.
- [5] Z. He, F. Gou, R. Chen, K. Yin, T. Zhan, S. T. Wu, *Crystals* **2019**, *9*, 292.
- [6] Y. H. Lee, K. Yin, S. T. Wu, *Opt. Express* **2017**, *25*, 27008.
- [7] J. Kobashi, H. Yoshida, M. Ozaki, *Phys. Rev. Lett.* **2016**, *116*, 253903.
- [8] M. G. Nassiri, S. Y. Cho, H. Yoshida, M. Ozaki, E. Brasselet, *Phys. Rev. A* **2018**, *98*, 063834.
- [9] J. Kobashi, H. Yoshida, M. Ozaki, *Mol. Cryst. Liq. Cryst.* **2017**, *646*, 116.
- [10] M. Rafayelyan, G. Agez, E. Brasselet, *Phys. Rev. A* **2017**, *96*, 043862.
- [11] K. Yin, H. Y. Lin, S. T. Wu, *Opt. Express* **2019**, *27*, 35895.
- [12] K. J. Hornburg, J. Kim, M. J. Escuti, *Proc. SPIE* **2017**, *10125*, 101250Y.
- [13] M. Khorasaninejad, W. T. Chen, R. C. Devlin, J. Oh, A. Y. Zhu, F. Capasso, *Science* **2016**, *352*, 1190.
- [14] H. Liang, A. Martins, B.-H. V. Borges, J. Zhou, E. R. Martins, J. Li, T. F. Krauss, *Optica* **2019**, *6*, 1461.
- [15] J. Kim, Y. Li, M. N. Miskiewicz, C. Oh, M. W. Kudenov, M. J. Escuti, *Optica* **2015**, *2*, 958.
- [16] K. Gao, H. H. Cheng, A. K. Bhowmik, P. J. Bos, *Opt. Express* **2015**, *23*, 20.
- [17] P. Chen, B. Y. Wei, W. Hu, Y. Q. Lu, *Adv. Mater.* **2019**, *31*, 1903665.
- [18] S. Wang, P. C. Wu, V. C. Su, Y. C. Lai, M. K. Chen, H. Y. Kuo, B. H. Chen, Y. H. Chen, T. T. Huang, J. H. Wang, R. M. Lin, *Nat. Nanotechnol.* **2018**, *13*, 227.

- [19] J. Y. Lee, B. H. Hong, W. Y. Kim, S. K. Min, Y. Kim, M. V. Jouravlev, R. Bose, K. S. Kim, I. C. Hwang, L. J. Kaufman, C. W. Wong, *Nature* **2009**, 460, 498.
- [20] M. Hoffmann, B. Judkewitz, *Optica* **2019**, 6, 1166.
- [21] Y. H. Lee, G. Tan, K. Yin, T. Zhan, S. T. Wu, *J. Soc. Inf. Disp.* **2018**, 26, 64.
- [22] Y. H. Lee, Z. He, S. T. Wu, *J. Opt. Soc. Am. B* **2019**, 36, D9.
- [23] J. Xiong, R. Chen, S. T. Wu, *Opt. Express* **2019**, 27, 18102.
- [24] G. Crawford, J. Eakin, M. Radcliffe, A. Callan-Jones, R. Pelcovits, *J. Appl. Phys.* **2005**, 98, 123102.
- [25] L. Nikolova, T. Todorov, *Opt. Acta* **1984**, 31, 579.
- [26] K. Yin, Y. H. Lee, Z. He, S. T. Wu, *Opt. Express* **2019**, 27, 5814.
- [27] K. Yin, Y. H. Lee, Z. He, S. T. Wu, *J. Soc. Inf. Disp.* **2019**, 27, 232.
- [28] Z. He, Y. H. Lee, K. Yin, S. T. Wu, *Proc. SPIE* **2019**, 11092, 1109204.
- [29] O. Yaroshchuk, H. Gurumurthy, V. G. Chigrinov, H. S. Kwok, H. Hasebe, H. Takatsu, *Proc. IDW* **2007**, 7, 1665.
- [30] J. West, S. Linli, Y. Reznikov, *Mol. Cryst. Liq. Cryst. Sci. Technol., Sect. A* **2001**, 364, 199.
- [31] D. K. Yang, S. T. Wu, *Fundamentals of Liquid Crystal Devices*, 2nd ed., John Wiley & Sons, Chichester, UK **2014**.